Locally symmetric oxygen vacancy around Cd impurities in CeO_2

W. L. Ferreira,* L. F. D. Pereira, O. F. S. Leite Neto, L. S. Maciel, V. C. Gonçalves, R. N. Saxena, and A. W. Carbonari†
Instituto de Pesquisas Energéticas e Nucleares-IPEN-CNEN/SP, São Paulo, Brazil

M. S. Costa
Faculdade de Ciências Exatas e Tecnologia, Universidade Federal do Pará-UFPA, Brazil

G. A. Cabrera-Pasca
Programa de Pós-graduação em Ciência e Engenharia de Materiais, Universidade Federal do Pará-UFPA, Brazil

(Received 31 August 2020; revised 11 June 2021; accepted 1 July 2021; published 23 July 2021)

A detailed investigation of the electronic structure in the neighborhood of Cd impurities in CeO_2 has been performed by *ab initio* calculations to elucidate the interplay between the oxygen vacancies and electric quadrupole interactions. The quadrupole frequency related to the major component of the electric-field gradient (EFG) at impurities sites from its neighboring charge density as well as its symmetry were calculated by simulating oxygen vacancies at oxygen nearest neighbor of Cd. Results show a very good agreement with experimental hyperfine interactions measurements at the ^{111}Cd nucleus replacing Ce at CeO_2. A systematic mapping of oxygen vacancies in CeO_2 supercells was proposed within the framework of density-functional theory using the WIEN2K code focusing on the electronic distribution in the vicinity of Cd impurities. Results show that the calculated values of EFG crucially depend on impurity-vacancy complex position and the striking axial symmetry observed when an oxygen monovancy is at the nearest neighborhood of Cd is explained by a rearrangement of its *p* orbitals.

DOI: 10.1103/PhysRevB.104.035146

I. INTRODUCTION

Among the most common oxide systems that crystallize in the fluorite structure (e.g., UO_2, ZrO_2, and ThO_2), CeO_2 (ceria) has received wide attention in the scientific community regarding its phase transitions and the nature of the intrinsic point defects arising from the loss of oxygen. In early investigations [1–3], several phases at low temperatures were found from the neutron diffraction and conventional x-ray diffraction (XRD) studies. More recently, a larger number of phases were reported from which a complete phase diagram was constructed by Zinkevich *et al.* [4] by reanalyzing the experimental data from various sources. The phase diagram draws attention immediately to the presence of a wide-range single phase that remains thermodynamically stable even under extreme conditions of pressure and temperature. This offers a great opportunity to study solid-state properties in CeO_2 with small and large concentrations of defects and could also allow an assessment of the dynamics of point defects in crystalline sites and local properties close to them.

Although the nonstoichiometry of a metal oxide may be the result of a series of defects, such as cation vacancy, interstitial oxygen, interstitial cations, dopants, among others, the earlier studies seem to converge to an oxygen vacancy model. Steele and Floyd [5] measured oxygen self-diffusion in both CeO_2 and $CeO_{(2-y)}$ solutions, and concluded that oxygen vacancies are clearly the predominant defect. Ban and Nowick [6] investigated the effects of reducibility on CeO_{2-y} monocrystals and did not observe any significant changes in the size of crystallites and the magnitude of the lattice parameters. This result is consistent only with a vacancy model. Considering the mass action law, Blumenthal and Garnier [7] measured the electrical conductivity (σ) from 1073 to 1773 K over a wide range of $p(O_2)$ and noted that their results are consistent with a defect model involving oxygen vacancies and hopping-type conductivity due to the presence of impurities and/or stoichiometric deficiency. It is noteworthy that later experiments performed by Tuller and Nowick [8] showed to be the clearest case of small polaron hopping conductivity. Barker *et al.* [9] carried out conductivity measurements at high temperature (from 973 to 1273 K) and low pressure, showing a dependence of σ on $p(O_2)^{-1/5}$, suggesting a mechanism based on the formation of oxygen monovacancies $V_O^{\cdot\cdot}$ and oxygen divacancies $2V_O^{\cdot\cdot}$ (in Kroger-Vink notation) [10].

Afterwards, with increased scientific and technological progress, more attention was given to the prediction and design of materials which motivated a growing interest in ceria. Robust theoretical-computational approaches and well-established experimental techniques have been used in an unprecedented way in the investigation of ceria defects. Consequently, fundamental questions, such as the nature of the chemical bonding in CeO_2 and key concepts, such as the occupation of the $4f$ orbital have been extensively discussed. In this context two possibilities have been taken into account:

*wlferreira@usp.br
†carbonar@ipen.br

 ©2021 American Physical Society

(i) The valence band (VB) is completely unoccupied, showing an ionic bond between Ce and O (all valence electrons of the Ce will be transferred to the O-2p band). (ii) The valence band is partially occupied, and the Ce-O pair assumes a covalent bond character (all four Ce electrons participate in the bond) where ionicity is less than four. Koelling *et al.* [11], using the linearized augmented-plane wave method determined the CeO_2 band structure. The results show that the model which assumes the Ce-4f to be partially occupied provides a good prediction of the electronic structure and properties related to the ground state and found that the Ce-4f electron population in CeO_2 was 0.5. The existence of hybridization between Ce and O valence bands was revealed from density of state (DOS) calculations. Wuilloud *et al.* [12] suggest that in CeO_2, there is only +1.92 charge in the Ce valence band (less than half the +4 formal charge). The estimated Ce-4f electron population is approximately 0.8 corresponding to a predominantly ionic bonding character, thus, constituting a mixed valence state model, which is strongly supported by experimental results [13–15]. From the point of view of practical interest the high mobility of oxygen in the crystal lattice is another subject which has been widely investigated. This dynamic process according to Skorodumova *et al.* [16] is closely related to the 4f-electron (de)localization. In this paper, the authors suggest that in the formation of $V_O^{\cdot\cdot}$, two electrons are left behind, so that a perfect electron localization always occurs on the 4f of two Ce ions that are nearest neighbors (NN) to the defect.

The formation and migration of defects due to local disorder of oxygen vacancies in ceria has not been completely understood despite an extensive number of experimental and theoretical studies. The local disorder originated from oxygen vacancies and doping has been the aim of several studies in which hyperfine interactions techniques, in particular, time differential perturbed angular correlation (PAC) spectroscopy due to its extreme sensitivity to even small structural changes is known to be a great tool for investigation. Wang *et al.* [17] were the pioneers in investigating pure ceria by PAC using ^{111}Cd as a probe in the temperature range from 77 to 1073 K. They reported three different quadrupole interaction (NQI) frequencies reflecting the existence of three nonequivalent probe sites: One "site *A*" was characterized as a complex formed by the Cd-$V_O^{\cdot\cdot}$ pair, and two different "site *B*" and "site *C*" related to Cd-2$V_O^{\cdot\cdot}$ pairs. For measurements up to 276 K, they observed evidence of a dynamic process due to the transmutation produced by the nuclear electron capture (EC) [^{111}In(EC)/ ^{111}Cd], giving rise to the electronic relaxation process usually called electron capture decay after effects (ECAE) [18–20]. Some time later, Requejo *et al.* [21] also performed PAC measurements in pure CeO_2 using ^{181}Ta. They show that initial PAC data in the temperature range from 77 to 300 K exhibited an unperturbed cubic environment suggesting that the probe does not trap vacancies. They observed that defects were promoted by long thermal treatment at 1323 K at low oxygen pressure of 0.01 Torr. In sequence, PAC measurements revealed the presence the two interactions that have been attributed to oxygen vacancies and the presence of a possible rhombohedral phase.

Considering the conflicting results reported for the NQI [17,21], we intend to elucidate the origin of the electric hyperfine interactions and improve the understanding about the role of impurities in oxygen vacancy formation in ceria through *ab initio* calculations and complementary PAC measurements. Hence, this paper presents the following: (i) In the experimental approach, a protocol for preparing the CeO_2 sample was developed using Pechini-type sol-gel process. The probe nuclei ^{111}Cd were introduced during the sample preparation, and annealing treatment was performed in order to mobilize defects and favor substitutional replacement of Ce by Cd. The XRD technique was used for structural characterization of the sample. The PAC measurements were performed to determine the hyperfine parameters of interest and confirm the results reported by Wang *et al.* [17], and (ii) the theoretical and computational approaches were confined to structural optimization, fundamental properties, such as eletronic DOS and the prediction of the electric-field gradient (EFG) tensor. These calculations were carried out using the WIEN2K code [22] where a series of Cd-doped CeO_2 "superstructures" with periodic boundary conditions were modeled for the mapping of defects considering different possible anion site positions for creating oxygen monovacancies and divacancies.

II. EXPERIMENTAL DETAILS

Polycrystalline CeO_2 was prepared by the well-known sol-gel method as follows: High-purity Ce metal was dissolved in a small quantity of aqua regia. Stoichiometric quantities of citric acid and ethylene glycol were added to the cerium solution with constant stirring at 353 K until the formation of the gel which was sintered at 823 K for 12 h in air to form the CeO_2 powder. The powder was then annealed at 1273 K for 10 h. The sample was characterized by XRD and analyzed by the Rietveld method. The sample for PAC measurements was prepared using the same procedure as above except that approximately 50 μCi of the radioactive indium chloride ($^{111}InCl_3$) solution were added to Ce solution before the gel formation.

PAC measurements were carried out using the 171–245-keV γ cascade in ^{111}Cd from the decay of ^{111}In in the temperature range from 77 to 773 K using a conventional slow-fast coincidence setup with a spectrometer consisting of four BaF_2 scintillator detectors in a planar 90° arrangement. The system allows to obtain simultaneously 12 coincidence spectra $N(\theta,t)$ eight recorded at angles $\theta = 90°$ and four at 180°. More details about the experiment procedure and treatment of data can be obtained from Refs. [23,24]. The EFG is defined as the second derivative of a classical electrostatic potential with respect to Cartesian coordinates $V_{ij} = \partial^2 V/\partial x_i \partial y_j$ at the nuclear position. PAC probes situated in different lattices sites of a sample are likely to experience different values of EFG. In addition to the magnitude V_{zz} of the tensor, which is related to the quadrupole frequency $\nu_Q = eQV_{zz}/h$, the anisotropy parameter $\eta = (V_{xx} - V_{yy}/V_{zz})$ that varies from 0 to 1, is also needed for the complete characterization of EFG. From the measured coincidence spectra, the time-differential anisotropy $R(t)$ can be calculated

$$R(t) = A_{22}^{\text{eff}} \sum_i f_i G_{22}^i(t) = 2\frac{N(180°,t) - N(90°,t)}{N(180°,t) + 2N(90°,t)}. \quad (1)$$

Here, A_{22}^{eff} is the effective anisotropy of the angular correlation of γ cascade [25], f_i are the fractions of different sites occupied by the probe nuclei and $G_{22}^i(t)$ are the corresponding perturbation functions describing the time modulation of the angular correlation. The appropriate time-differential perturbation function can be written as follows:

$$G_{22}^i(t) = e^{-\lambda t}\left(S_{20} + \sum_{n=1}^{3} S_{2n}(\eta^i)\cos\left[\omega_n^i(\eta^i)t\right]e^{-\delta_Q^i\omega_n^i t}\right), \quad (2)$$

where, the transition frequencies ω_n^i are related to the hyperfine splitting of the intermediate level of the of the probe. The dynamic attenuation parameter (λ) takes in to account the EFG fluctuations within the observation of PAC timescale. Description of the PAC method can be found elsewhere [26–28].

III. COMPUTATIONAL METHOD

Following the procedure described by Cottenier [29], a Wigner-Seitz cell with the crystallographic parameters extracted from the XRD measurements has been used as starting the CeO_2 structure. For investigating different possibilities of defect complexes in Cd-doped bulk ceria, we have used a periodic supercell (SC) model. Initially, a structure with only one-point symmetry operation ($C_1 = \{E\}$) was chosen which modeled a standard supercell containing 96 nonequivalent atoms (32 Ce and 64 O atoms) from $2 \times 2 \times 2$ replication of the conventional 12-atom face-centered cubic unit cell of CeO_2 one Ce atom was replaced by a Cd atom, corresponding to a dopant concentration of 3% (which is sufficiently large for hyperfine interactions calculations). According to the illustration made in the VESTA software [30] and displayed in Fig. 1, there are different possible anion site positions for creating defect complex. We have analyzed the cases where the oxygen monovacancy and divacancy are located, respectively, at 1NN and 2NN with respect to the Cd ion.

For monovacancy modeling [Fig. 1(a) when $V_O^{\cdot\cdot}$ is located at 1NN (111), the Cd site is coordinated with seven equivalent oxygens when $V_O^{\cdot\cdot}$ is located at 2NN (112), the Cd site is coordinated with eight equivalent oxygens. For the divacancy model [Fig. 1(b)], the supercell with $V_O^{\cdot\cdot}$ at 1NN is adopted for modeling a new standard supercell where that monovacancy is taken as fixed (gray sphere in Fig. 1), but due to the symmetry transformations it was allocated from the plane (111) to $(11\bar{1})$. The new structure generated has one more point symmetry operation ($C_s = \{\sigma_h, \sigma_h^2 = E\}$) than its predecessor where the Cd site surrounded by seven oxygens is arranged into nonequivalent geometric configuration: The onefold coordinated oxygen atom is located at plane $(\bar{1}\bar{1}1)$. Threefold coordinated oxygen atoms on the planes (111) and $(\bar{1}\bar{1}\bar{1})$. Thus, it is necessary to remove only one oxygen from each plane for the complete mapping of oxygen divacancies.

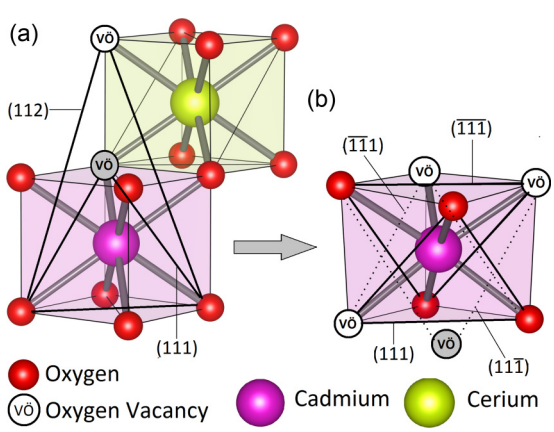

FIG. 1. A schematic of the impurity sites of the various supercell models of this paper. (a) Impurity site with the possibility of formation of $V_O^{\cdot\cdot}$ in different anionic coordinations [first nearest neighbor (1NN) and second nearest neighbor (2NN)]. (b) Impurity site with $2V_O^{\cdot\cdot}$ at 1NN.

In order to investigate the mechanism of defects in these supercells, the theoretical calculations based on the density functional theory (DFT) formalism, have been performed with the full potential linearized augmented plane wave plus local orbital (APW+lo) method [31] as embodied in the WIEN2K code [22] where the exchange and correlation (XC) effects were described through the generalized gradient approximation (GGA) in the parametrization of Perdew-Burke-Ernzerhof (PBE) [32]. Since there are no shape approximations to the charge density (or to the potential) in a multipole expansion of the Coulomb potential from $L = 2$, $M = 0$ value at $r = 0$, we can calculate the main component of EFG by [33]

$$V_{zz} = \left(\frac{5}{4\pi}\right)\lim_{r\to 0}\left[\frac{V_0^2(r)}{r^2}\right], \quad (3)$$

where V_0^2 is the radial potential coefficient, which is solved numerically using the Rudge-Poisson equation, whose solution to the boundary value problem is obtained by the method proposed by Weinert [34],

$$V_0^2 = -C_0^2\int_0^{R_{MT}}\frac{\rho_0^2(\vec{r})}{r}dr + C_0^2\int_0^{R_{MT}}\frac{\rho_0^2(\vec{r})(r/R_{MT})^5}{r}dr + 5C_0^2\sum_K V(K)J_2(KR_{MT})Y_0^2(\hat{K}), \quad (4)$$

with $C_0^2 = 2(4\pi/5)^{1/2}$, J_2 is the spherical Bessel function, Y_0^2 is the spherical harmonic. The first term in Eq. (4) is named as the valence contribution of EFG arising from the nonspherical electron density of the valence and semicore electrons into muffin-tin (MT) spheres of radius R_{MT}. The second term appears when solving the boundary value problem to ensure continuity of the potential at $r = R_{MT}$. The third term comes from the charge density outside the MT spheres. The sum of the second and third terms represents the lattice contribution of EFG. In Eq. (4), the double sum of the wave functions with angular momentum (l or l') for radial coefficient $\rho_0^2(\vec{r})$ takes into account only the following combinations of l and l' are allowed (see Ref. [35]): $p - p$, $s - d$ (this term is negligible), and $d - d$ (here $d - d$ represents a "pure" d-electron density whose contribution to V_{zz} comes from electrons with strong d character). According Schwarz *et al.* [36], the theoretical valence EFGs can be related to the symmetry-decomposed

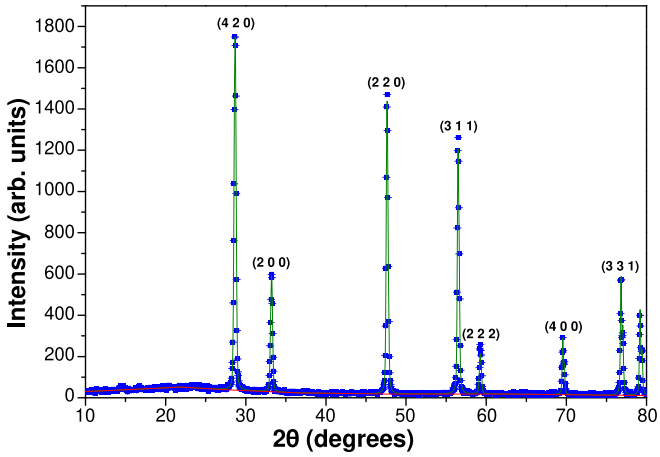

FIG. 2. XRD in a powder sample at room temperature for pure CeO_2. The solid lines represent the calculated XRD pattern using the Rietveld method.

charges inside the muffin-tin sphere, reflecting in the so-called asymmetry count. This parameter is defined for p and d charges, respectively, as

$$\Delta n_p = \tfrac{1}{2}\left(n_{p_x} + n_{p_y}\right) - n_{p_z}, \tag{5}$$

$$\Delta n_d = \left(n_{d_{xy}} + n_{d_{x^2-y^2}}\right) - \tfrac{1}{2}\left(n_{d_{xz}} + n_{d_{yz}}\right) - n_{d_{z^2}}, \tag{6}$$

with n_{p_i} and $n_{d_{ij}}$, respectively, are the number of electrons in the p_i orbital and d_{ij} orbital. The EFG computation depends on the basis set size ($R_{MT}^{\min} K_{\max}$), the number of irreducible k points, the accuracy of the convergence criteria, the XC functional, and the structure (i.e., atom arrangement, ratio of lattice constants, etc.). The computational details are now summarized.

The following R_{MT} values are used for the Ce, Cd, and O, respectively: 2.19, 2.17, and 1.95 arb. units. The convergence of the basis set is controlled by a cutoff parameter $R_{MT}^{O} K_{\max} = 7$. The k-point sampling of the Brillouin zone was evaluated in the regular Monkhorst-Pack scheme [37] using a $4 \times 4 \times 4$ k-mesh grid. The integration of k space was performed by linear tetrahedron method with Bloechl corrections and the temperature broadened smearing parameter of 0.001 eV to deal with damp oscillations in the self-consistency cycle. Since Ce^{+4} and Cd^{+2} have different covalent and ionic radii and considering the presence of oxygen vacancies, a significant lattice distortion is expected, therefore, we have performed geometry optimization with reverse-communication trust-region quasi-Newton routine [38] to ensure that the atomic positions are fully relaxed until Hellmann-Feynman forces on atoms are smaller than 0.01 eV/Å. Taking into account a possible deep impurity acceptor level in the band gap of the host when a Ce^{+4} is substituted by Cd^{+2} as well as the formation of oxygen vacancies, we have also performed calculations for different charge states of the impurity.

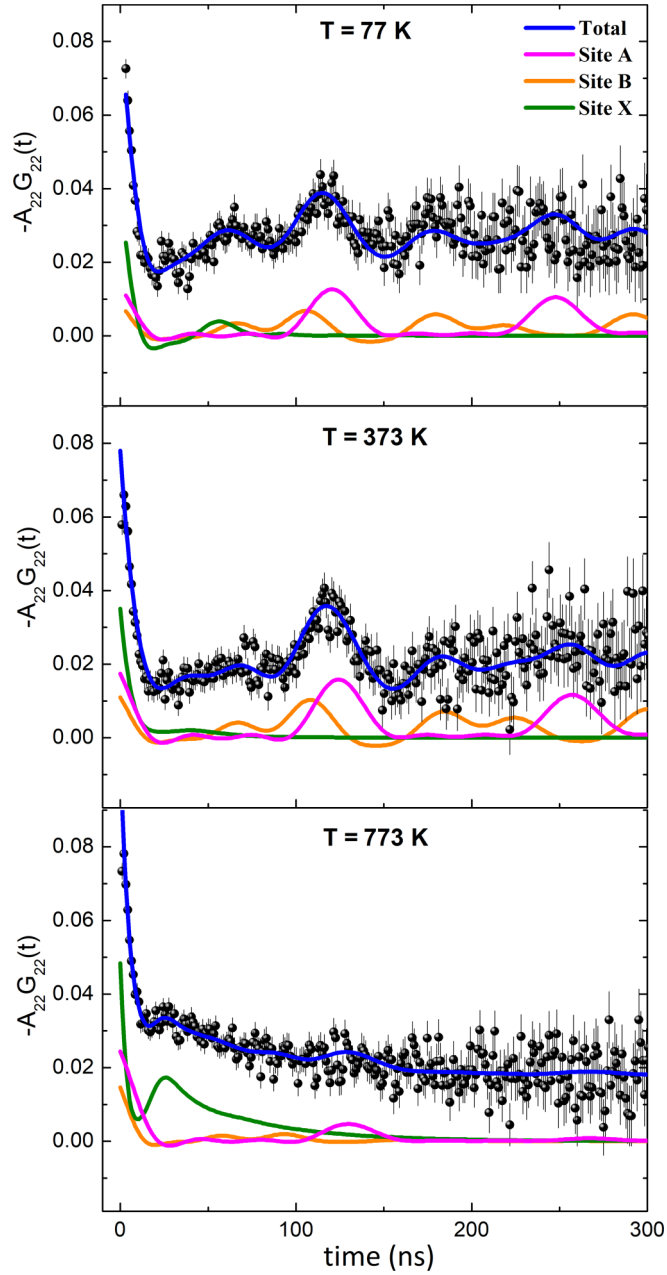

FIG. 3. PAC spectra of CeO_2 at temperatures indicated. The solid lines represent the fits to the theoretical function discussed in the text.

IV. RESULTS AND DISCUSSION

A. XRD and PAC results using ^{111}Cd probe nuclei

The XRD spectra are shown in Fig. 2 for the CeO_2 sample measured at room temperature. The results confirm the fluorite structure. The diffractogram was analyzed by the Rietveld method. The XRD peaks (see Fig. 2) exhibit small broadening, which indicates good crystallinity. The lattice parameter obtained is $a = 5.404$ Å, being in excellent agreement with experimental results [1,39]. The mean grain size is 141 nm (obtained from the Scherrer [40] formula).

The result of PAC measurements at the indicated temperatures, Fig. 3, show that the ^{111}Cd probes sense an unexpected NQI since CeO_2 crystallizes in the cubic fluorite structure one

TABLE I. Hyperfine parameters obtained from the PAC spectra as a function of temperature.

Site	T (K)	f (%)	ν_Q (MHz)	η	δ (%)	λ (MHz)
A	298	13.0	53.2	0.1	1.9	0
B	298	8.0	61.1	0.40	2.4	0
X	298	79.0	117.0	1.00	0	86.2
A	373	15.0	53.6	0.1	3.1	0
B	373	9.5	59.2	0.4	3.2	0
X	373	76.0	133.0	1.0	0	114.2
A	773	29.0	0	0	0	16.2
B	773	3.0	84.8	0.5	0	0
X	773	68.0	108.4	1.0	0	104.7

should not expect perturbations in the angular correlation due to the NQI in the intermediate state of the γ cascade in ^{111}Cd. Therefore, we need possible explanation for the existence of NQI in the CeO_2 sample.

An important feature of the PAC spectra is the fast damping of the angular correlation pattern near the origin of the timescale. We attribute such behavior to time-dependent local charge distribution around the probe nuclei, giving rise to a dynamic change in the EFG. This stochastic behavior was included in the fit with the model according to Eq. (2). The PAC data were interpreted in terms of three NQI frequencies corresponding to probe nuclei occupying different site fractions in CeO_2. Two of the fractions have well-defined NQI frequencies (called sites A and B) and were assigned to the ^{111}Cd probes occupying substitutional Ce sites with different environments localized in the core of the grain of ceria. The third site (named site X) presents a strong damping of the amplitude and most probably corresponds to ^{111}Cd situated in the grain boundary. Experimental hyperfine parameters obtained from the PAC measurements are shown in Table I.

The result of site A ($f = 13.0\%$) are in excellent agreement with the site A reported by Wang *et al.* [17] where at room temperature they obtained the quadrupole frequency $\nu_q = 53.05$ MHz with $\eta = 0$. This axially symmetric site was associated by the authors to the trapped oxygen monovacancy at the first neighbor or second neighbor of the probe nucleus. Considering that the $^{111}Cd^{+2}$ ion should act as a double acceptor impurity to substitute Ce^{+4} will give it a -2 negative charge. Thus, in order not to have the electron-hole formation, a doubly charged oxygen vacancy will be enhanced to satisfy a charge neutrality condition. The low-frequency interaction for site A probably should be attributed to a local lattice relaxation. The other defect complex, the site B ($f = 8.0\%$) is also in excellent agreement with site B of Wang *et al.* [17] with $\nu_q = 63$ MHz and $\eta = 0.35$. The authors speculated that this asymmetric site, considering its low interaction frequency, could be a complex with one vacancy in a first- and one in a second-neighbor position as the small size of the probe permits a large lattice relaxation. Moreover, they show that this site B and a third site C in their experiment only appeared when they performed an annealing for 0.5 h at 1473 K and pressure $p(O_2) = 5$ mTorr. In this paper, site C was not observed, which may indicate a lower concentration of trapped oxygen vacancies around cationic sites in our sample. Finally, it is assumed that the majority site X ($f = 79\%$) comes from a grain boundary contribution. Physical considerations support this hypothesis, Wang *et al.* [17] in a preliminary work produced ceria samples with calcination at 1273 K, much higher temperatures than that used in this paper, reported PAC results indicating a considerable concentration of ^{111}Cd that does not correspond to the the bulk crystal. The significant fraction of sites with ^{111}Cd in grain boundary regions was reduced with ceria calcinated at 1473 K. Higher-temperature calcination produced a substantial increase in grain size of ceria to 10 μm.

Above 573 K the quadrupole frequency for site A drops to zero as expected and observed by Wang *et al.* [17], indicating that the local structure around the ^{111}Cd probe is perfectly crystalline without defects. Values of λ were only observed for temperatures above 573 K for site A, whereas for site X the values increase up to 573 K and then decrease. Differently from Wang *et al.* [17], dynamic interaction was not observed for site B.

The observation of dynamic interactions is a consequence of a regime where EFG is fluctuating in time produced by ionic (oxygen vacancy) and electronic (electron and electron-hole) charges. In the case of sites A and B, the dominant contribution to EFG most likely comes from trapped oxygen vacancies in the core of the ceria grain where we can assume the existence of compensation of holes by electrons released from oxygen vacancies that are uniformly arranged around the probe sites, and a stable electronic configuration is reached where ν_Q changes little with temperature. In the scenario of site X, the EFG contribution in grain boundary is expected to be mainly electronic. Tschöpe [41] confirmed that in ceria at a grain size of ~600 nm the depletion of oxygen vacancies is stronger than of electron holes. In addition, taking into account the lower crystallinity in the grain boundaries, an unstable physical situation occurs in this region: With increasing temperature a trapping and detrapping of electron holes in the close neighborhood of the ^{111}Cd tracers favors the ECAE followed by the Auger cascade which leaves the probe nucleus in a highly ionized state, affecting the angular correlation and, therefore, expressive changes in ν_Q at high temperatures.

B. *Ab initio* DFT calculations

Before performing calculations to obtain the hyperfine properties we have first optimized the structural parameters of the pure CeO_2 unit cell. These data were fitted (Fig. 4) using the Birch-Murnaghan equation of state [42].

According to the inset image of Fig. 4, the volume equilibrium per formula unit (V_0/f.u.) predicted by APW + lo is about 4% greater than the experimental value (266.246/f.u Å) extracted from our XRD measurements, which in terms of the cubic lattice parameter corresponds to a difference of about 1.2%. As for predictions of bulk modulus (B) and its derivative of pressure (B'), one can see that, in general, our results are within the expected range of those predicted in the literature by DFT calculations [43–45] or experimental results [46,47], whose set of B values obtained in the measurements depends on the sample morphology as well of the conditions of the environment acting during the experiment.

In this paper, the major component of the EFG tensor calculated within the framework of the APW + lo ($V_{zz}^{\rm calc}$) comes

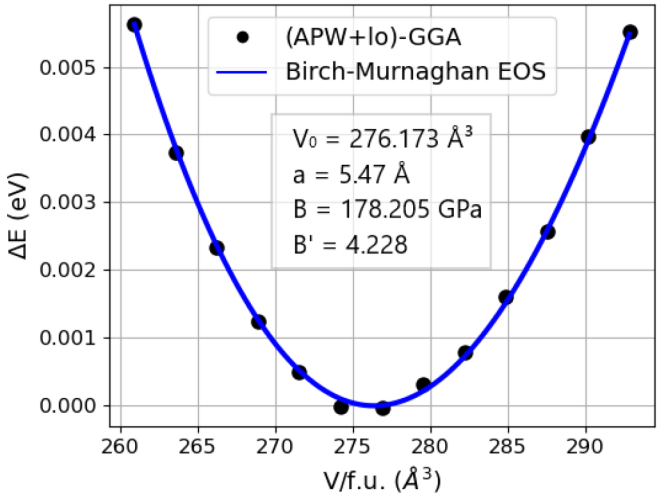

FIG. 4. Dependence of the ΔE for pure CeO_2 on volume (black circles) of its unit cell. The blue solid line corresponds to the fit data.

from the p and d orbitals (V_{zz}^{p} and V_{zz}^{d}). The term V_{zz}^{exp} is the experimental value of V_{zz} extracted from PAC results. The estimation of V_{zz}^{exp} from the experimental quadrupole frequencies (ν_Q or ω_1) and the asymmetry parameter (only for ω_1) depends on the electric quadrupole moment (Q) of the ^{111}Cd intermediate level of 245 keV. Values of Q reported in the literature vary within a wide range and, consequently, can strongly affect V_{zz}^{exp} leading to a misinterpretation of the calculated V_{zz}^{calc}; few examples can be found in the compilation by Stone [48]. A detailed description of all reported values in the literature as well as a comparison between them, displayed in a nice graph, were reported by Errico *et al.* [49] The most quoted value is $Q = 0.83(13)$ b reported by Herzog *et al.* [50], whereas the newest value is $Q = 0.664(7)$ b reported by Haas *et al.* [51], which give an idea of the amplitude of the difference between the values. Here we have adopted $Q = 0.765(15)$ b, one of the most recent reported values [52] which is equal to the also recent value reported by Errico *et al.* [49] and is within a narrower range that includes the reliable experimental values (for details, see the compilation in Ref. [49]).

As mentioned earlier, the supercell approach was used to investigate point defects that give rise to EFG in ceria. In the EFG analysis, we considered two set of internal structure parameters: The experimental atomic positions (unrelaxed supercell) and theoretical equilibrium atomic positions (relaxed supercell). Considering the double acceptor character of Cd^{+2} in the ceria host, these substitutional defects can introduce lack of charges, inducing an electron-density recombination which can strongly affect the EFG around of Cd, putting at stake the real charge state of the impurity that corresponds to the experimental results. Therefore, for EFG analysis a charge compensation (nucleus versus electrons) study was undertaken. We performed the systematic mapping of point defects in order of complexity. First, we simulated an ideal scenario where a Ce atom was replaced by Cd in the supercell without the ionic defects, i.e., oxygen vacancies, according to what was described previously in Sec. III. For this, we have performed calculations assuming a "neutral charge state" ($q = 0$) and adding electrons to the SC (due to differences in valence between Ce and Cd) in $1e^-$ steps up to $2e^-$ (i.e., $q = -1$ and $q = -2$).

TABLE II. Final distances, d(Cd-O$_n$) in angstroms of Cd to its O-1NN in unrelaxed and relaxed supercells of $Ce_{0.97}Cd_{0.03}O_2$ considering three charge states.

	Unrelaxed supercell			Relaxed supercell		
d(Cd-O$_n$)	$q = 0$	$q = -1$	$q = -2$	$q = 0$	$q = -1$	$q = -2$
d(Cd-O$_1$)		2.37		2.42	2.44	2.46
d(Cd-O$_2$)		2.37		2.42	2.44	2.46
d(Cd-O$_3$)		2.37		2.42	2.44	2.46
d(Cd-O$_4$)		2.37		2.42	2.44	2.46
d(Cd-O$_5$)		2.37		2.42	2.44	2.46
d(Cd-O$_6$)		2.37		2.42	2.44	2.46
d(Cd-O$_7$)		2.37		2.42	2.44	2.46
d(Cd-O$_8$)		2.37		2.42	2.44	2.46

The APW + lo predictions show that the EFG is null at the Cd impurity site and does not depend on the charge state considered, and ceria does not present any significant local disorder around the probe. This is seen more clearly in Table II where the bond lengths after full structural relaxation increase isotropically in the system, thus, preserving the cubic-octahedral symmetry of the cationic site. This situation was experimentally achieved when measuring temperature increases, and probably the lattice relaxes to the cubic symmetry. The expansion in the bond lengths produced by Cd at the Ce site are related to the fact that the ionic radii for eightfold coordinated Cd^{+2} (1.1 Å) is greater than the ionic radii for eightfold coordinated Ce^{+4} (0.97 Å) [53]. This expansion of all oxygen atoms around Cd is also connected with the Coulomb repulsion due to the extra charge added in the system. Therefore, an electron-density recombination occurs where the probe does not trap one or two electron holes, consistent with a nonzero EFG. This *ab initio* results are compatible with hyperfine parameter behavior of the sites A and B of our PAC results in which the probe nucleus decays reaching to the final neutral (stable) charge state ($^{111}Cd^{+2}$) before or during the PAC time window, being practically free of ECAE. However, despite its consistency in the combined experimental—*ab initio* approach, this SC is too simplistic to support a compensatory effect of electron-holes suggested via PAC measurements since the crystalline defects that give rise to EFG are formed in the nucleation process of ceria grains.

In a second step we have carried out a mapping of oxygen monovacancy ($V_O^{\cdot\cdot}$) in ceria. Since our PAC data and previous *ab initio* calculations seems to justify the validity of a charge-compensation mechanism via electron density recombination where the residual charge from $V_O^{\cdot\cdot}$ is compensated by the possible lack of charges arising from the substitutional defect (Ce by Cd), we, therefore, have not assumed different charge state possibilities. Since the cationic sites of standard SC are axially symmetric, only the removal of an extra oxygen to account for the nonzero EFG experimentally observed from each neighborhood is necessary to map it completely.

The EFG computation results (see Table III) successfully predict the experimental hypothesis of oxygen monovacancy trapped by a Cd at the 1NN with $V_{zz}^{\text{calc}} = 2.76 \times 10^{21}$ V m^{-2}

TABLE III. Hyperfine parameters predicted for $Ce_{0,97}Cd_{0,03}O_{1,97}$ at the Cd site in unrelaxed and relaxed supercells considering the oxygen monovacancy formation possibility at 1NN and 2NN. V_{zz} is in units of 10^{21} V m^{-2}.

	Unrelaxed supercell		Relaxed supercell	
EFG	$V_O^{\cdot\cdot}$ at (111)	$V_O^{\cdot\cdot}$ at (112)	$V_O^{\cdot\cdot}$ at (111)	$V_O^{\cdot\cdot}$ at (112)
V_{zz}^p	2.83	0.51	1.29	2
V_{zz}^d	3.84	0.12	1.47	0.55
V_{zz}^{calc}	**6.67**	**0.63**	**2.76**	**2.55**
Δn_p	0	0	0	0.001
Δn_d	0	0.001	0	0.011
η	0	0.12	0	0.52
PAC this paper: Site A $\{V_{zz}^{\text{exp}} = 2.81;\ \eta = 0.1\}$.				
PAC Ref. [17]: Site A $\{V_{zz}^{\text{exp}} = 2.87;\ \eta = 0\}$.				

and $\eta = 0$. Wang *et al.* [17] suggested that the value obtained of $V_{zz}^{\text{exp}} = 2.87 \times 10^{21}$ V m^{-2} could be justified by large lattice relaxation due the small size of the Cd. As we can be seen in Table III, we have predicted $V_{zz}^{\text{calc}} = 6.67 \times 10^{21}$ V m^{-2} for the supercell with the experimental atomic positions, however, the relaxation introduced by the impurity decreases the V_{zz}^{calc} value by a factor of more than 2.4. This result is consistent with the increase in Cd-O_n displacements observed in Table IV. In electrostatic terms our calculations corroborate that due to a $1/r^3$ dependency of the EFG tensors, the presence of $V_O^{\cdot\cdot}$ causes an increase in Coulomb repulsion between Cd and O_n.

The contributions to V_{zz} from p and d electrons changes significantly when the oxygen vacancies are at 1NN and at 2NN (see Table III). The behavior is different when comparing the unrelaxed with the relaxed supercell. For 1NN, V_{zz} decreases for both p and d electrons when the unrelaxed lattice is considered, whereas for 2NN a correspondent increase is observed. This can be explained by the the fact that Cd-d and Cd-p electrons interact strongly with the oxygen p electrons in valence band, thereby a small change in the electron-density distribution in these p states with oxygen vacancy at 2NN influences the EFG at Cd sites where the corresponding asymmetry count ($\Delta n_p = 0.001$, $\Delta n_d = 0.011$) in relaxed supercell can be attributed, respectively, to a depletion of p_z, d_{z^2}, and $d_{x^2-y^2}$ charges, indicating an $\eta \neq 0$. On the other hand, the spherical symmetry in the ceria system with $V_O^{\cdot\cdot}$ at 1NN leads to $\Delta n_p = \Delta n_d = 0$ (i.e. $n_{p_x} = n_{p_y} = n_{p_z}$, $n_{d_{xy}} = n_{d_{xz}} = n_{d_{yz}}$ and $n_{d_{x^2-y^2}=d_{z^2}}$) and, consequently, $\eta = 0$. Thus, due to the covalent interaction, this deviation from cubic symmetry in the Cd-d and Cd-p electrons can be interpreted as a reexpansion of the O-p orbital tails entering the Cd sphere, that is extremely sensitive to 1NN Cd-O coordination. In the following, we demonstrate this clear relation with EFG.

When the $V_O^{\cdot\cdot}$ is located at the 2NN of the Cd probe site there is a decrease in V_{zz}^{calc} with a consequent loss of the axial symmetry, as expected. Since this oxygen removed from 2NN (122 position in Fig. 1) was being shared between two Ce atoms, the oxygen at the opposite position (O_8), which is shared between the Cd and Ce atoms, consequently, O_8 is attracted by the neighboring Ce and it is displaced by moving away from the Cd atom in such a way that there is an increase in the Cd-O_8 distance of about 15%. The distances of the other seven oxygen atoms in the Cd cell (Cd-O_{1-7}) increase around 10%, and considering the extreme sensitivity of the EFG with the distance, this discrepancy is sufficient to obtain an asymmetry at the probe site of $\eta = 0.52$.

Continuing the mapping of impurity-defect complexes, we have modeled supercells containing two oxygen vacancies ($2V_O^{\cdot\cdot}$). Wang *et al.* consider the formation of oxygen divacancies around the ^{111}Cd probe site to explain PAC results [17]. Specifically, it is possible to consider several positions of both oxygen vacancies, which can be the most favored positions, e.g., 1NN:1NN, 1NN:2NN, 1NN:3NN, or more complicated situations, e.g., 2NN:2NN, 3NN:3NN. We have considered *a priori* two nearest oxygen divacancy (1NN-1NN) with three possible two-vacancy $2V_O^{\cdot\cdot}$ configurations. For hyperfine parameters calculations, in addition to the neutral ($q = 0$) condition, "charged states" have also been taken into account at the limit where the sum of nuclear charges and electronic charges must cancel, that is, removing charges $q = +1$ and $q = +2$ of the SC. The EFG results at the Cd sites are listed in the Table V. As can be seen, the EFG in the scenarios with $2V_O^{\cdot\cdot}$ at $(11\bar{1})$:(111) and $(11\bar{1})$:$(\bar{1}\bar{1}1)$, respectively, are in excellent agreement with the experimental values for Sites B and C reported in PAC results.

The results of calculations indicate that due to vacancy-vacancy interactions (or perhaps a modification of the lattice at high vacancy levels), in general, the relaxation effects are not so expressive in EFG computation, except for the supercell with $2V_O^{\cdot\cdot}$ at $(11\bar{1})$:(111) where the value of η at the probe site decreases with the process of structural relaxation. On the other hand, EFG values, in particular, the major component V_{zz} at the probe site, depend strongly on the positions occupied by vacancies where local structural modifications have a great influence on the distribution of p-character charges, being small when the pair of vacancies is located at $(11\bar{1})$:(111) and becoming dominant when divacancy is at the $(11\bar{1})$:(111) position.

It is worth highlighting the role of Cd-d electrons in the EFG because the d shell tends to be fully occupied, this charge

TABLE IV. Final distances, d(Cd-O_n) in angstroms, of Cd to its O-1NN in unrelaxed and relaxed supercells of $Ce_{0.97}Cd_{0.03}O_{1.97}$ considering the oxygen monovacancy formation possibility at 1NN and 2NN.

	Unrelaxed supercell		Relaxed supercell	
d(Cd-O_n)	$V_O^{\cdot\cdot}$ at (111)	$V_O^{\cdot\cdot}$ at (112)	$V_O^{\cdot\cdot}$ at (111)	$V_O^{\cdot\cdot}$ at (112)
d(Cd-O_1)	2.37	2.37	2.36	2.41
d(Cd-O_2)		2.37		2.42
d(Cd-O_3)	2.37	2.37	2.39	2.43
d(Cd-O_4)	2.37	2.37	2.39	2.46
d(Cd-O_5)	2.37	2.37	2.39	2.46
d(Cd-O_6)	2.37	2.37	2.44	2.46
d(Cd-O_7)	2.37	2.37	2.44	2.46
d(Cd-O_8)	2.37	2.37	2.44	2.73

TABLE V. Hyperfine parameters predicted for $Ce_{0.97}Cd_{0.03}O_{1.94}$ at the Cd site in unrelaxed and relaxed supercells considering the oxygen divacancy formation possibilities at 1NN. V_{zz} is in units of 10^{21} V m^{-2}. The sign of the experimentally determined V_{zz} is unknown.

	Unrelaxed supercell			Relaxed supercell		
EFG	$q=0$	$q=+1$	$q=+2$	$q=0$	$q=+1$	$q=+2$
			$2V_O^{\cdot\cdot}$ at $(11\bar{1})$:(111)			
V_{zz}^p	−1.32	−1.91	−1.92	−1.54	−1.46	−1.13
V_{zz}^d	−2.37	−2.82	−2.82	−2.09	−2.06	−2.02
V_{zz}^{calc}	**−3.7**	**−4.72**	**−4.73**	**−3.54**	**−3.52**	**−3.15**
Δn_p	0	−0.001	−0.001	0	−0.001	−0.001
Δn_d	−0.001	−0.002	−0.002	−0.002	−0.002	−0.001
η	0.87	0.97	0.97	0.26	0.33	0.37
			$2V_O^{\cdot\cdot}$ at $(11\bar{1})$:$(\bar{1}\bar{1}\bar{1})$			
V_{zz}^p	4.29	2.57	4.04	3.31	4.22	4.24
V_{zz}^d	3.28	3.44	4.32	2.98	2.84	2.84
V_{zz}^{calc}	**6.71**	**6.01**	**8.36**	**6.29**	**7.06**	**7.08**
Δn_p	0.004	0.002	0.005	0.004	0.007	0.007
Δn_d	0	0.001	0.002	0	0.002	0.001
η	0.04	0.09	0.05	0.03	0.15	0.13
			$2V_O^{\cdot\cdot}$ at $(11\bar{1})$:$(\bar{1}\bar{1}1)$			
V_{zz}^p	4.64	9.23	7.46	7.64	7.5	7.68
V_{zz}^d	4.23	0.62	4.03	3.96	3.87	4
V_{zz}^{calc}	**8.81**	**9.85**	**11.49**	**11.6**	**11.37**	**11.68**
Δn_p	0.024	0.022	0.022	0.021	0.02	0.021
Δn_d	0.004	0.007	0.008	0.008	0.007	0.008
η	0	0.04	0.04	0.02	0.03	0.01

PAC this paper: Site B $\{V_{zz}^{\text{exp}} = 3.30; \eta = 0.40\}$.
PAC Ref. [17]: Site B $\{V_{zz}^{\text{exp}} = 3.21; \eta = 0.35\}$.
Site C $\{V_{zz}^{\text{exp}} = 12.3; \eta = 0\}$.

distribution should have spherical symmetry and, therefore, its participation in V_{zz} should be negligible. However, the strong interaction of O-2p with Cd-d states induces an anisotropy in the charge distribution, generating significant contributions to V_{zz}^d, whose well-balanced values over the three possible divacancy positions occur due a slightly asphericity in the electron-density distribution of the valence electrons from Cd-p_x, Cd-p_y, and Cd-p_z orbitals. As can also be seen in Table V, the variation of Δn_p is significantly greater than Δn_d where it is observed that all these values of asymmetry count are proportional the magnitude and the sign of the V_{zz}^p and V_{zz}^d contributions.

In all theoretical values listed in Table VI, it is possible to observe a clear correlation between η values and the NN Cd-O coordination where the supercell with oxygen divacancy configuration $(11\bar{1})$:$(\bar{1}\bar{1}\bar{1})$ has the most isotropic distances in the first coordination of the probe site. This correspond to the most symmetrical Cd site containing oxygen divacancy, consequently, it has the smallest values of η (cf. Table V). Furthermore, after the structural relaxation, the distances decrease, that is, we have an attractive Coulomb effect. This result can be explained by the fact that with the loss of two oxygens, the probe site is now coordinated by six oxygens, following a general trend already observed in binary oxides doped with Cd with different crystalline structures in which the impurity of the Cd tries to reconstruct the length of the 2.35 Å Cd-O bond of its most stable oxide the CdO [54] where the cationic site is coordinated by six anions.

In order to understand how the impurity levels affect the band structure of the ceria, we predict the DOS composition, shown in Fig. 5 for the VB at the energy above of −6 eV and below 6 eV from the bottom of the conduction band (CB). It is noteworthy that we used the atomic positions at theoretical equilibrium for the DOS and those scale factors in order to better visualize the PDOS with respect to TDOS contributions. In a pure unit cell, Fig. 5(a), the characteristic band with width of around −3.5 eV, is mainly formed by O-2p states, being in good agreement with experimental [12,55] results as well as *ab initio* calculations [11]. It can be noted that the prominent sharp peak that define the CB bottom as expected is dominated by Ce-4f states.

Another important feature is the band admixtures, i.e., hybridization between O-2p and Ce-4f states, evidencing a predominant covalent bond character. This raises an issue: the Ce valence and the presence of part of 4f band in the valence band. The band gap is about 2 eV, reproducing the typical wide gap semiconductor feature of the ceria, however, this value is underestimated in comparison to the experimental gap estimate of 3 eV, which is expected for pure DFT XC functionals. Hence, our calculations show that a strict band-gap description (even with the presence of intrinsic and extrinsic

TABLE VI. Final distances, $d(\text{Cd-O}_n)$ in angstroms of Cd to its O-1NN in unrelaxed and relaxed supercells of $Ce_{0.97}Cd_{0.03}O_{1.94}$ considering the oxygen divacancy formation possibilities at 1NN.

	Unrelaxed supercell			Relaxed supercell		
$d(\text{Cd-O}_n)$	$q=0$	$q=+1$	$q=+2$	$q=0$	$q=+1$	$q=+2$
		$2V_O^{\cdot\cdot}$ at $(11\bar{1})$:(111)				
$d(\text{Cd-O}_2)$		2.39		2.35	2.35	2.36
$d(\text{Cd-O}_3)$		2.39		2.35	2.35	2.36
$d(\text{Cd-O}_4)$		2.39		2.36	2.36	2.36
$d(\text{Cd-O}_5)$		2.44		2.36	2.36	2.37
$d(\text{Cd-O}_6)$		2.44		2.37	2.36	2.37
$d(\text{Cd-O}_7)$		2.44		2.37	2.37	2.37
		$2V_O^{\cdot\cdot}$ at $(11\bar{1})$:$(\bar{1}\bar{1}\bar{1})$				
$d(\text{Cd-O}_1)$		2.35		2.32	2.32	2.31
$d(\text{Cd-O}_3)$		2.39		2.34	2.32	2.32
$d(\text{Cd-O}_4)$		2.39		2.36	2.34	2.35
$d(\text{Cd-O}_5)$		2.44		2.36	2.36	2.36
$d(\text{Cd-O}_6)$		2.44		2.38	2.37	2.36
$d(\text{Cd-O}_7)$		2.44		2.38	2.37	2.37
		$2V_O^{\cdot\cdot}$ at $(11\bar{1})$:$(\bar{1}\bar{1}1)$				
$d(\text{Cd-O}_1)$		2.35		2.31	2.32	2.32
$d(\text{Cd-O}_2)$		2.39		2.31	2.32	2.32
$d(\text{Cd-O}_3)$		2.39		2.38	2.38	2.37
$d(\text{Cd-O}_4)$		2.39		2.38	2.38	2.37
$d(\text{Cd-O}_5)$		2.44		2.39	2.40	2.41
$d(\text{Cd-O}_7)$		2.44		2.39	2.40	2.41

point defects) is not crucial in the prediction of electric hyperfine interactions at the Cd site.

Moreover, Richard *et al.*, have investigated the effect of $4f$ electrons on the EFG at Cd-impurity nuclei at rare-earth sites in a comprehensive theoretical study in rare-earth sesquioxides [56]. The reported results indicate that the EFG systematics predicted by local spin-density approximation (LSDA) is qualitatively the same as those predicted by LSDA $+ U$. This standard DFT approach has been successfully applied in the prediction of the electric hyperfine properties for a broader range of oxide systems [19,57,58], consolidating a benchmark set that validates the use of standard local or semilocal functionals, even if the approximation does not hold exactly a rigorous description of the localization effects.

Regarding the substitution of a Ce atom by a Cd impurity as can be seen by comparing Figs. 5(b) and 5(c), the DOS peaks are very similar for both non-neutral $Ce_{0.97}Cd_{0.03}O_2$ SC. As a result, the extra charges added to the system are uniformly distributed, i.e., the Cd impurity does not act as a trapping site of charges. Considering the possibility of small-polaron formation which has been largely reported for ceria these results can be understood as Cd impurity does not act as a self-trapped polaron. This substitutional defect makes the VB transpose the Fermi level, signaling the onset of a metallic ground-state behavior (that is better shown in magnifications of the DOS on the right side of corresponding figures). According to PDOS, the complete dilution of impurity levels of a minority Cd-$4d$ state in the VB is in fine agreement with the picture of Cd as a double acceptor impurity in ceria. However, as can be seen comparing the TDOS predictions in Figs. 5(b) and 5(c) with the TDOS for $Ce_{0.97}Cd_{0.03}O_{1.97}$ SC, [Fig. 5(d)], the referred highest occupied band moves directly below the Fermi level. This phenomenon is clearly induced after the introduction of the oxygen monovacancy. In the sequence, considering the DOS composition in Fig. 5(e) for $Ce_{0.97}Cd_{0.03}O_{1.94}$ SC, one can see a localization effect of the CB bottom, leveraging a mixed valence state model regime with partly filled Ce-$4f$ state situated right at the Fermi level and an increase in the number of states/eV in the VB. From a hyperfine interactions perspective, the increase in δ peaks, mainly in the Ce-$4f$ states, this change in the electron energy levels is an indication of lattice distortions in the crystal that lead to anisotropy in the charge distributionthus, leading to a nonzero EFG at the cation sites. This behavior occurs mainly due the Ce-$4f$ and O-$2p$ states that obtain electrons arising from the oxygen divacancy, thus, having a decrease in their respective energies. Yang *et al.* [59] using DFT $+ U$, reported a similar DOS result for unreduced and reduced Pd-doped ceria systems where a band localization effect is observed with the formation of oxygen vacancy. Finally, taking into account the charge balance after removing two electrons from the $Ce_{0.97}Cd_{0.03}O_{1.94}$ SC, the DOS composition in Fig. 5(f) exhibits a delocalization effect whose energy ranges for the VB and CB become similar to the DOS composition of the $Ce_{0.97}Cd_{0.03}O_{1.97}$ SC [Fig. 5(d)]. At this point, the charge effects shown in Figs. 5(e) and 5(f) for $Ce_{0.97}Cd_{0.03}O_{1.94}$ SC, could be related to the polaron-$V_O^{\cdot\cdot}$ interactions. Whereas it is widely accepted that polarons play a relevant role on the local structure in reduced ceria as reported recently [60–62], however, based on the excellent concordance between our DFT calculations and the PAC experiments for the EFG parameters, we have obtained a quantitative verification that the polaron effects on the local structure at Cd impurity sites in reduced ceria are very small. Therefore, the binding of a polaron to oxygen vacancies and its associated Cd impurity is unfavorable. Considering the polaron formation in materials most likely occurs with electrons of incomplete d or f inner shells, therefore, polaron effects do not play an essential role in our methodology for mapping of oxygen vacancies. Therefore, we can assume that these APW + lo calculations at the GGA level correctly describe the electronic structure in the framework of electric quadrupole interactions for impurity-host systems studied in this paper.

V. CONCLUSIONS

Through *ab initio* DFT calculations and results from PAC spectroscopy, we have obtained an appreciable insight for the understanding of the electronic structure of CeO_2 in the context of hyperfine interactions, focusing on the study of the origin of the EFG in the vicinity of Cd. The correlation between PAC and DFT calculations reveals that Cd doping promotes oxygen monovacancy and divacancy at the nearest neighbors in the lattice. In this paper, polycrystalline CeO_2 was prepared by the sol-gel process and had their structure and composition characterized by XRD. From the PAC measurements, we characterized three nonequivalent probe sites: Two impurity-defect complexes, sites A and B, that we, respectively, attributed to the presence of oxygen monovacancies

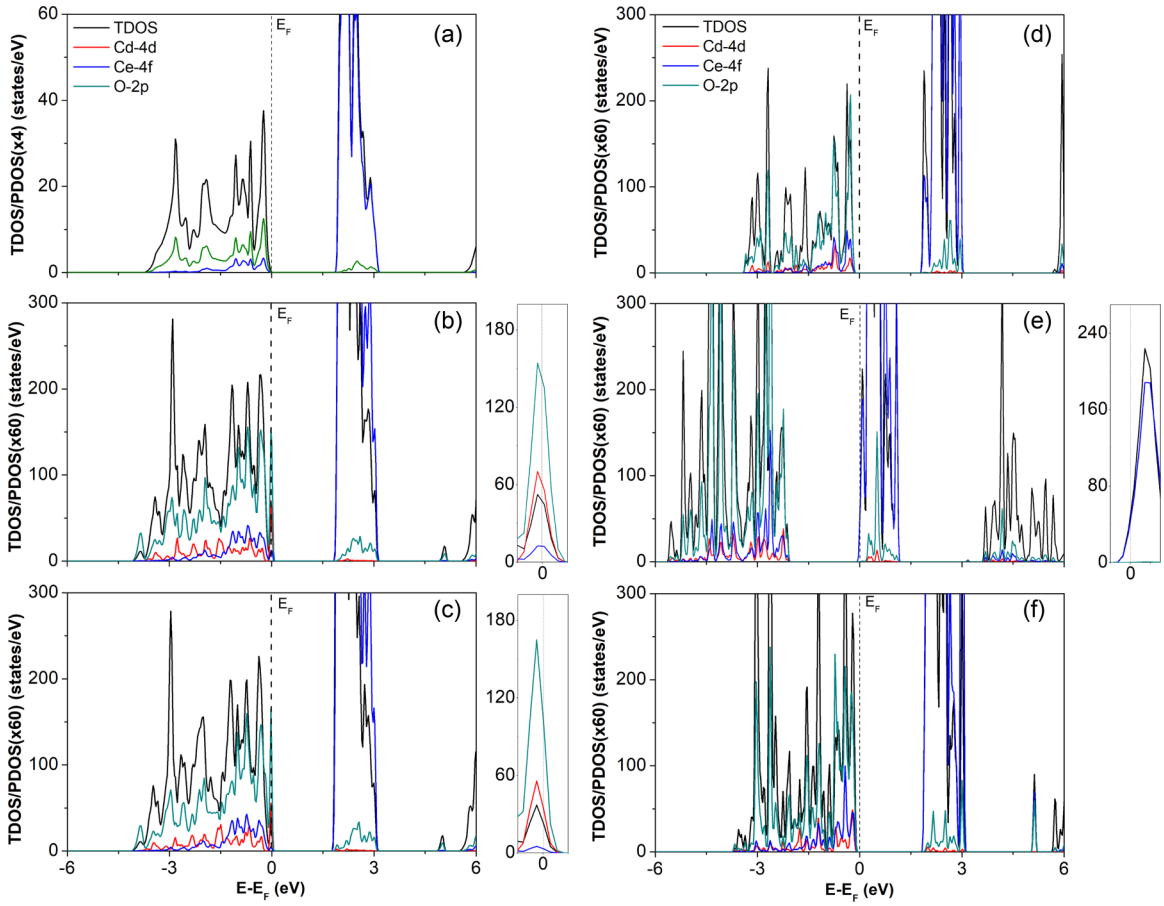

FIG. 5. Calculated total DOS (TDOS) and most relevant partial DOS (PDOS) predicted by GGA-PBE for (a) CeO_2, (b) $Ce_{0.97}Cd_{0.03}O_2$ SC in charge state $q = 0$, (c) $Ce_{0.97}Cd_{0.03}O_2$ SC in charge state $q = +2$, (d) $Ce_{0.97}Cd_{0.03}O_{1.97}$ SC with $V_O^{\cdot\cdot}$ at (111), (e) $Ce_{0.97}Cd_{0.03}O_{1.94}$ SC with $2V_O^{\cdot\cdot}$ at $(11\bar{1})$:$(\bar{1}\bar{1}1)$ in charge state $q = 0$, (f) $Ce_{0.97}Cd_{0.03}O_{1.94}$ SC with $2V_O^{\cdot\cdot}$ at $(11\bar{1})$:$(\bar{1}\bar{1}1)$ in charge state $q = -2$. The Fermi level (E_F) is indicated by the vertical dot line at 0 eV and different scales were used on the y axis for greater clarity in all graphs.

and oxygen divacancies situated at the 1NN of the probe. These two sites are in excellent agreement with the present PAC results as well as those of the literature [17]. The third interaction, corresponds to the majority of site X, characterized by a strong dynamic interaction, which we associate with oxygen vacancies in the grain boundaries, this site is, therefore, strongly influenced by *after effects*. The comparison between these experimental results and the corresponding DFT calculations demonstrates the reliability of these theoretical studies where such predictions contributed to elucidate the structural and electronic processes caused by point defects, confirming the preponderant role of a aliovalent ion in the formation of locally symmetric oxygen vacancy complexes that give rise to EFG in ceria, an aspect that until now has been very little explored in the literature.

ACKNOWLEDGMENTS

Partial financial support for this work was provided by the Fundação de Amparo a Pesquisa do Estado de São Paulo (FAPESP) under Grant No. 2014/14001-1. W.L.F. acknowledges Coordenação de Aperfeiçoamento de Pessoal de Nível Superior (CAPES) for financial support in a form of scholarship (Grant No. 88882333432/2019-01) and L.S.M. and A.W.C. acknowledge the Conselho Nacional de Desenvolvimento Científico e Tecnológico (CNPq) for financial support (Grants No. 134233/2017-4 and No. 304627/2017-8, respectively). L.F.D.P. expresses his thanks CNPq for financial support in a form Fellowship (Grant No. 444323/2018-0 of the Programa de Capacitação Institucional-PCI). G.A.C.-P. gratefully acknowledges support from the CNPQ (via Grant No. 430060/2018-1).

[1] D. J. M. Bevan, J. Inorg. Nucl. Chem. **1**, 49 (1955).
[2] G. Brauer and K. A. Gingerich, J. Inorg. Nucl. Chem. **16**, 87 (1960).
[3] S. P. Ray, A. S. Nowick, and D. E. Cox, J. Solid State Chem. **15**, 344 (1975).
[4] M. Zinkevich, D. Djurovic, and F. Aldinger, Solid State Ionics **177**, 989 (2006).
[5] B. C. H. Steele and J. M. Floyd, Proc. Brit. Ceramic. Soc. **19**, 55 (1971).
[6] Y. Ban and A. S. Nowick, Proc. 5th Materials Res. Symp. Spec. Publ. **364**, 353 (1972).
[7] R. N. Blumenthal and J. E. Garnier, J. Solid State Chem. **16**, 21 (1976).

[8] H. L. Tuller and A. S. Nowick, J. Solid State Chem. **38**, 859 (1977).
[9] E. H. Baker, M. Iqbal, and B. E. Knox, J. Mater. Sci. **12**, 305 (1977).
[10] F. A. Kröger and H. J. Vink, Solid State Phys. **3**, 307 (1956).
[11] D. D. Koelling, A. M. Boring, and J. H. Wood, Solid State Commun. **47**, 227 (1983).
[12] E. Wuilloud, B. Delley, W.-D. Schneider, and Y. Baer, Phys. Rev. Lett. **53**, 202 (1984).
[13] A. Fujimori, Phys. Rev. B **27**, 3992 (1983).
[14] A. Fujimori, Phys. Rev. B **28**, 2281 (1983).
[15] R. C. Karnatak, J. M. Esteva, H. Dexpert, M. Gasgnier, P. E. Caro, and L. Albert, Phys. Rev. B **36**, 1745 (1987).
[16] N. V. Skorodumova, S. I. Simak, B. I. Lundqvist, I. A. Abrikosov, and B. Johansson, Phys. Rev. Lett. **89**, 166601 (2002).
[17] R. Wang, J. A. Gardner, W. E. Evenson, and J. A. Sommers, Phys. Rev. B **47**, 638 (1993).
[18] P. Lehmann and J. Miller, J. Phys. Radium **17**, 526 (1956).
[19] G. N. Darriba, E. L. Muñoz, A. W. Carbonari, and M. Rentería, J. Phys. Chem. C **122**, 17423 (2018).
[20] J. Schell, D. C. Lupascu, J. G. M. Correia, A. W. Carbonari, M. Deicher, M. B. Barbosa, R. D. Mansano, K. Johnston, I. S. Ribeiro, and ISOLDE Collaboration, Hyperfine Interact. **238**, 2 (2017).
[21] F. G. Requejo, A. G. Bibiloni, C. P. Massolo, and K. Freitag, Modern Phys. Lett. B **8**, 329 (1994).
[22] P. Blaha, K. Schwarz, G. Madsen, D. Kvasnicka, and J. Luitz, WEN2K*: An Augmented Plane Wave Plus Local Orbitals Program for Calculating Crystal Properties* (Technische Universität Wien, Austria, 2001).
[23] R. Dogra, A. C. Junquiera, R. N. Saxena, A. W. Carbonari, J. Mestnik-Filho, and M. Moralles, Phys. Rev. B **63**, 224104 (2001).
[24] C. Sena, M. S. Costa, E. L. Muñoz, G. A. Cabrera-Pasca, L. F. D. Pereira, J. Mestnik-Filho, A. W. Carbonari, and J. A. H. Coaquira, J. Magn. Magn. Mater. **387**, 165 (2015).
[25] Y. A. Ellis, Nucl. Data Sheets **9**, 319 (1973).
[26] H. Frauenfelder and R. M. Steffen, in *Alpha-, Beta-, and Gamma-Ray Spectroscopy*, edited by K. Siegbahn (North-Holland, Amsterdam, 1966), Vol. 2.
[27] T. Wichert, in *Semiconductors and Semimetals*, edited by M. Stavola (Elsevier, 1999), Vol. 51.
[28] M. Zacate and H. Jaeger, Defect Diffus. Forum **311**, 3 (2011).
[29] S. Cottenier, *Density Functional Theory and the Family of (L)APW-Methods: A Step-by-Step Introduction*, 2nd ed. (freely available at http://www.wien2k.at/reguser/textbooks) (2002–2013).
[30] K. Momma and F. Izumi, J. Appl. Crystallogr. **44**, 1272 (2011).
[31] O. K. Andersen, Phys. Rev. B **12**, 3060 (1975).
[32] J. P. Perdew, K. Burke, and M. Ernzerhof, Phys. Rev. Lett. **77**, 3865 (1996).
[33] P. Blaha, K. Schwarz, and P. Herzig, Phys. Rev. Lett. **54**, 1192 (1985).
[34] M. Weinert, J. Math. Phys. **22**, 2433 (1981).
[35] P. Blaha and K. Schwarz, Int. J. Quantum Chem. **23**, 1535 (1983).
[36] K. Schwarz, C. Ambrosch-Draxl, and P. Blaha, Phys. Rev. B **42**, 2051 (1990).
[37] H. J. Monkhorst and J. D. Pack, Phys. Rev. B **13**, 5188 (1976).
[38] L. Marks, Optimization notes (available at http://www.wien2k.at/reg-user/textbooks/) (2004).
[39] M. Yashima, S. Kobayashi, and T. Yasui, Solid State Ionics **177**, 211 (2006).
[40] B. D. Cullity, *Elements of X-ray Diffraction* (Addison-Wesley, Reading, MA, 1956).
[41] A. Tschöpe, J. Electroceramics **14**, 5 (2005).
[42] F. Birch, Phys. Rev. **71**, 809 (1947).
[43] L. Gerward, J. S. Olsen, L. Petit, G. Vaitheeswaran, V. Kanchana, and A. Svane, J. Alloys Compd. **400**, 56 (2005).
[44] V. Kanchana, G. Vaitheeswaran, A. Svane, and A. Delin, J. Phys.: Condens. Matter **18**, 9615 (2006).
[45] Z. Yang, T. K. Woo, M. Baudin, and K. Hermansson, J. Chem. Phys. **120**, 7741 (2004).
[46] S. J. Duclos, Y. K. Vohra, A. L. Ruoff, A. Jayaraman, and G. P. Espinosa, Phys. Rev. B **38**, 7755 (1988).
[47] L. Gerward and J. S. Olsen, Powder Diffr. **8**, 127 (1993).
[48] N. J. Stone, J. Phys. Chem. Ref. Data **44**, 031215 (2015).
[49] L. Errico, K. Lejaeghere, J. Runco, S. N. Mishra, M. Rentería, and S. Cottenier, J. Phys. Chem. C **120**, 23111 (2016).
[50] P. Herzog, K. Freitag, M. Reuschenbach, and H. Walitzki, Z. Phys. A **294**, 13 (1980).
[51] H. Haas, J. Röder, J. G. Correia *et al.*, Phys. Rev. Lett. **126**, 103001 (2021).
[52] H. Haas and J. G. Correa, Hyperfine Interac. **198**, 133 (2010).
[53] L. H. Ahrens, Geochim. Cosmochim. Acta **2**, 155 (1952).
[54] R. W. G. Wyckoff, *Crystal Structures* (Interscience, New York, 1963), Vol. 1.
[55] F. Marabelli and P. Wachter, Phys. Rev. B **36**, 1238 (1987).
[56] D. Richard, E. L. Muñoz, M. Rentería, L. A. Errico, A. Svane, and N. E. Christensen, Phys. Rev. B **88**, 165206 (2013).
[57] G. N. Darriba, L. A. Errico, P. D. Eversheim, G. Fabricius, and M. Rentería, Phys. Rev. B **79**, 115213 (2009).
[58] G. N. P. Oliveira, R. C. Teixeira, R. P. Moreira, J. G. Correia, J. P. Araújo, and A. M. L. Lopes, Sci. Rep. **10**, 4686 (2020).
[59] Z. Yang, G. Luo, Z. Lu, and K. Hermansson, J. Chem. Phys. **127**, 074704 (2007).
[60] L. Sun, X. Huang, L. Wang, and A. Janotti, Phys. Rev. B **95**, 245101 (2017).
[61] D. Zhang, Z.-K. Han, G. E. Murgida, M. V. Ganduglia-Pirovano, and Y. Gao, Phys. Rev. Lett. **122**, 096101 (2019).
[62] C. W. M. Castleton, A. Lee, and J. Kullgren, J. Phys. Chem. C **123**, 5164 (2019).